In-situ measurements of contact evolution for fractal rough surfaces under normal compression

Shaoqi Huang [a,1], Deheng Wei [b,c,d,1], Wenwen Han [a], Hengxu Song [e,f], Siyang Song [a], Yixiang Gan [c,g], Chongpu Zhai [a,h,*], Minglong Xu [a,*]

[a] State Key Laboratory for Strength and Vibration of Mechanical Structure, School of Aerospace Engineering, Xi'an Jiaotong University, Xi'an, 710049, China
[b] Key Laboratory of Ministry of Education on Safe Mining of Deep Mines, School of Resources and Civil Engineering, Northeastern University, Shenyang, 110819, China
[c] School of Civil Engineering, The University of Sydney, NSW 2006, Australia
[d] Institute of Geomechanics and Underground Technology, RWTH Aachen University, Mies-van-der-Rohe-Str. 1, 52074 Aachen, Germany
[e] State Key Laboratory of Nonlinear Mechanics, Institute of Mechanics, Chinese Academy of Sciences, Beijing, 100190, China
[f] School of Engineering Science, University of Chinese Academy of Sciences, Beijing 100049, China
[g] Sydney Nano Institute, The University of Sydney, NSW 2006, Australia
[h] Shanxi Key Laboratory for Vibration and Control of Aerospace Structures, School of Aerospace Engineering, Xi'an Jiaotong University, Xi'an, 710049, China

ARTICLE INFO

ABSTRACT

The contact interface plays a key role in the overall functionality and stability of structures. Understanding the evolution of the contact interface over time and its dependency on materials and load is crucial for functional integrity and operational safety assessment. In this study, we employ in-situ three-dimensional X-ray computed tomography (3DXRCT) to examine the creep behavior of 3D-printed surfaces exhibiting various roughness under constant normal compression. We observe that the overall contact area enlargement during the contact creep decreases with roughness amplitude and fractal dimension. The variation of interfacial separation distance is found to increase with roughness amplitude and decrease with fractal dimension. Correlation analysis reveals that the microcontact size played a more important role than the asperity shape in determining the microcontact enlargement. By examining the calculated interfacial strains extracted from XRCT measurements, significant deformations are found to occur at the non-contacting zones, indicating strong asperity interactions. This study offers high-resolution experimental measurements and unravels the asperity micromechanics for contact creep on rough surfaces, providing insights into understanding and optimizing the performance of rough interfaces.

1. Introduction

Contacts between rough surfaces are ubiquitous in nature. The roughness creates a contact area formed by discrete microcontacts at the asperities (Yastrebov et al., 2015). These asperities usually exhibit distinct mechanical properties compared to the bulk, owing to their free surface or interactions among them. Therefore, the overall rough surface's mechanical responses depend on its surface roughness. Studying rough surface contact is crucial for assessing contact interface stability (Parland, 1995) and heat or electric conductance (Sevostianov and Kachanov, 2008), and is fundamental to friction-related studies (Popov et al., 2015).

Rough surface contact models can be classified into two main categories: Multi-asperity models (Greenwood and Williamson, 1966) and fractal models, including Persson's theory (Persson, 2001). The former strongly relies on the assumption of height and curvature distribution of roughness asperities, whereas the latter mainly deals with surfaces exhibiting fractality. Existing studies mostly utilize simple elastic or elastoplastic material constitutive models (Taylor, 2022) to simplify the model complexity. Although these models already satisfy the requirements of most engineering problems, there are cases when material viscosity strongly dominates mechanical responses, such as contact interfaces in long-service structures (Cecchi and Tralli, 2012); (He et al., 2021) or under extremely high temperatures (Barba et al., 2020). Examples include nuclear applications (Jia et al., 2020), turbines (Wang et al., 2016), electronic devices (Cholleti et al., 2021); (Depiver

et al., 2021), and earthquake-impacted geomaterials (Cristescu, 1993); (Michalowski et al., 2018). Under these circumstances, material creep must be considered for better assessment and design. Depending on the temperature, stress, and loading conditions, different mechanisms can contribute to creep behavior, including dislocation motion, chemical hardening, and bulk and boundary diffusion (Meng and Wang, 2019). Extensive research has been conducted on homogeneous bulk materials (Kassner, 2015); (Sandström, 2018); (Sofonea and Matei, 2012) to establish creep-related constitutive relations, such as exponential creep (Nix et al., 1985), power-law creep (Coble, 1963); (Conyers, 1950), and Garofalo creep (Garofalo, 1965). In contact mechanics, an expression for exponential creep dependence on stress has been proposed for hybrid analytical and experimental analyses of static friction coefficients (Brechet and Estrin, 1994). Brot et al. (2008) analytically derived the creep behavior of a single asperity in contact with a rigid plane, wherein the effects of holding time, normal load, and surface shape on a typical polymer material were investigated. They suggested that the contact area at a compressed asperity is linearly related to the product of the asperity radius and contact deformation, exhibiting a power-law dependence on time. Goedecke and Mock (Goedecke and Mock, 2009) proposed an expression for the time-dependent stress relaxation of a fully plastic asperity under fixed deformation using the Garofalo creep law (Garofalo, 1963), linking the power-law dependence of electrical contact resistance on time to contact creep (Goedecke et al., 2014). This power-law relationship between contact resistance and time was also supported by theoretical derivations and experiments by (Rezvanian et al., 2008). They observed two phases during contact creep of a single asperity, namely, a fast relaxation phase with a sharply increasing area, followed by a slow relaxation phase. The former was controlled by an increase in contact area, while the latter was dominated by strain hardening.

The effect of creep on the static friction coefficient was experimentally observed by Coulomb as early as the 1780s (Coulomb, 1785). In another notable pioneering study, (Spurr, 1955) demonstrated that the coefficient of friction increases in a power-law manner with respect to time. Current methods for evaluating contact area evolution include electrical conduction (Michopoulos et al., 2015); (Ta et al., 2021); (Zhai et al., 2017), stylus imaging (Pawlus et al., 2018); (Poon and Bhushan, 1995), optical microscopy (Li et al., 2021); (Merola et al., 2016); (Michalowski et al., 2018); (Ovcharenko et al., 2006); (Pawlus et al., 2017); (Pilvelait et al., 2020), and acoustic transmission (Dwyer-Joyce et al., 2001); (Gonzalez-Valadez and Dwyer-Joyce, 2009). For example, the influence of creep on microcontact adhesion of real radio frequency connectors was investigated using atomic force microscopy and laser vibrometry (Gregori and Clarke, 2006). (Gonzalez-Valadez et al., 2010) used an ultrasonic approach to experimentally study the interfacial stiffness of steel surfaces. Their results showed a power-law relationship between the contact stiffness and the time of contact creep. (Fu et al., 2018) conducted a creep test on a multilayer Ti/Al sample using nanoindentation, showing that microcontact creep also occurs visibly at room temperature. (Michalowski et al., 2018) reported that the time-dependent maturation process of silica sand particles under a constant compression load is significantly dependent on the initial surface roughness. By optically measuring the interface of a rough silicone rubber surface compressed by the smooth soda-lime glass, (Pilvelait et al., 2020) demonstrated that the real contact area of a frictional interface changes rapidly when the normal load is altered, and evolves slowly when the normal load is held constant. They also found that the time-dependent contact state is not entirely determined by the size of the real contact area but also by the geometrical features of the asperities.

Although the contact creep behavior has been reported in different experiments, existing experimental techniques have certain limitations. For example, interfacial electrical conduction, suffers from contamination films, oxide layer, and local heat build-up, hindering accurate and repeatable measurements. Stylus profilometer, optical, and acoustic methods are limited by their temporal and spatial resolutions.

Importantly, these methods only enable measurement of the established contact, but the deformation of non-contacting zones cannot be properly captured. With the development of X-ray detection technology, fast three-dimensional X-ray computed tomography (3DXRCT) has been employed to obtain 3D contact configurations of rough surfaces (Zhang et al., 2019), including both contacting and non-contacting zones. Recently, the combination of 3DXRCT and digital volume correlation (DVC) analysis has been applied to accomplish *in-situ* measurements of the microstructure evolution in cementitious composites (Hurley et al., 2023), providing a novel route for inferring micromechanics at rough contacts.

In this study, we employed 3DXRCT to examine the evolution of asperity deformation on rough fractal surfaces under a constant normal compression load. Using 3D-printed surfaces designed with targeted roughness features, we conducted 3DXRCT and quantified the variations in contact enlargement and interfacial separation distance over successive measurement steps with controlled time intervals. Through self-developed algorithms for image processing in 3D, each microcontact of the interface was segmented, labeled, characterized, and tracked. The roles of microcontact size and asperity shape in microcontact evolution were compared based on correlation analysis. Furthermore, we leveraged DVC analysis for mapping the full-field von Mises strain, to link local creep deformation with roughness characteristics. The findings can be applied to improve the design and performance of rough contacts in various engineering applications.

2. Experimental methodology

2.1. Sample preparation

The surface morphology plays a crucial role in determining how the roughness of a contact evolves. In this study, a series of 3D-printed rough surfaces exhibiting distinct geometries were experimentally tested to gain insights into the role of surface roughness on contact creep under constant normal compression by a flat silica block. The rough surfaces were simulated using a modified Weierstrass–Mandelbrot (WM) function (Yan and Komvopoulos, 1998) and 3D-printed by ProJet MJP 3600 Max (3D Systems) with a spatial printing resolution of approximately 16 μm, as shown in Fig. 1 (c). The cut-off wavelength in generating a rough surface with the WM function was also set to 16 μm, consistent with the 3D printing resolution. The 3D-printing material used was VisiJet Crystal, a UV-curable plastic, whose mechanical properties are listed in Table 1. In this study, we control two fundamental roughness descriptors, i.e., fractal dimension and roughness amplitude, which determine the hierarchical features and height scaling, respectively. More details on the surface generation and characterization are provided in Appendix A. The used material in this study exhibits mechanical properties close to a range of widely-used synthetic polymers (Alaboodi and Sivasankaran, 2018), including polyethylene terephthalate (PET), acrylonitrile butadiene styrene (ABS), Nylon66, etc. We examined the creep behavior under normal compression for five sample surfaces, as summarized in Table 2. The first group, including S1, S2 and S5, had the same R_t of 1 mm, but different values of $D_{in} \in \{2.1, 2.3, 2.5\}$; the second group, including S2, S3, and S4, had the same $D_{in} = 2.3$, but the roughness amplitude was $R_t \in \{1, 1.25, 1.5\}$ mm. The 3D-printed specimen diameter was 2.5 mm. A 0.5 mm thick substrate was included in the printing to ensure the overall flatness of the rough surfaces by increasing the resistance to bending. For the rough surfaces examined in this study, the prescribed R_t for surface generation can be nearly fully preserved in the 3D-printed samples. The characterized R_{rms} increases monotonically with R_t for a given fractal dimension D_{in}. For a given R_t, the characterized R_{rms} tends to decrease slightly with D_{in}. When both R_t and D_{in} are specified, generated surfaces exhibit certain fluctuations in characterized R_{rms}, as indicated by the standard deviation calculated across ten numerical realizations. The fractal dimension of a rough surface can be assessed by different methods (Nayak et al., 2019),
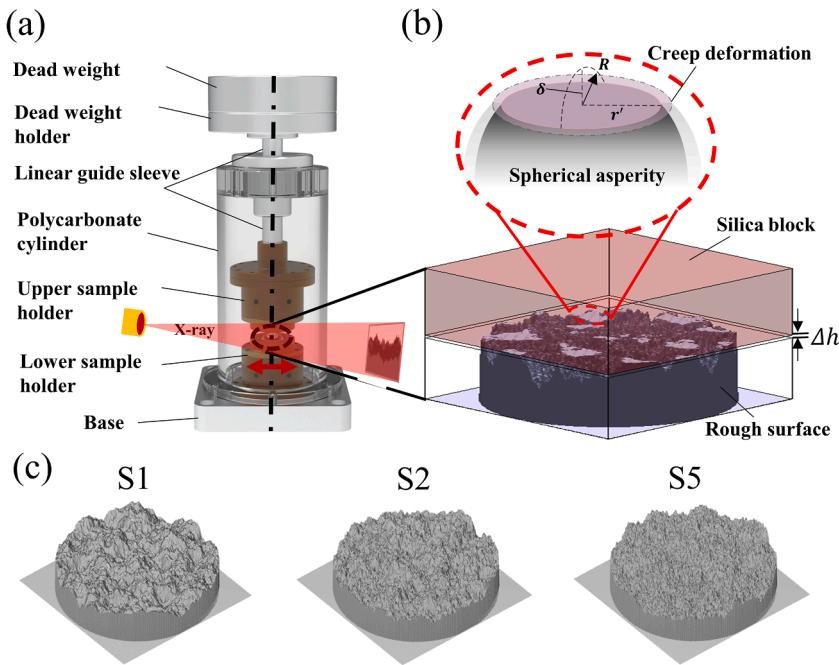
Fig. 1. (a) Schematic of the experimental setup. (b) The rough surface under normal compression. The inset indicates the simplified asperity deformation during contact creep. (c) Illustration of tested specimens with different surface roughness.

Table 1
Mechanical properties of contact materials.

Parameters	VisiJet Crystal (Alaboodi and Sivasankaran, 2018)	Silica
Elastic modulus E (GPa)	1.463	71.2
Poisson's ratio ν	0.30	0.30
Yield strength Y_0 (MPa)	42.4	80
Density ρ (g/cm^3)	1.02	2.65
Hardening exponent M	0.8	1
Creep exponent N	0.25	0

Table 2
Surface roughness characterizations of tested specimens before compression.

No.	D_{in}	$R_t/$ mm	D_{box}	$R_{rms}/$μm	XRCT resolution (μm)
S1	2.1	1.00	2.226 ± 0.008	148.105 ± 22.120	2.959
S2	2.3	1.00	2.323 ± 0.014	132.570 ± 23.190	3.304
S3	2.3	1.25	2.324 ± 0.008	162.871 ± 13.369	2.910
S4	2.3	1.50	2.321 ± 0.009	191.113 ± 21.933	2.910
S5	2.5	1.00	2.429 ± 0.006	125.953 ± 19.017	3.304

Note: D_{in} and R_t are prescribed parameters to Eq. (A1) to control, respectively, the hierarchical and vertical features of the generated surfaces. The actual fractal dimension and root-mean-square roughness of generated surfaces are further characterized using D_{box} and R_{rms}. The provided standard deviation is calculated over ten numerical realizations.

including the vertical sections method, power spectrum analysis, triangulation method, and box-counting method, etc. In Appendix A, we compare the calculated values of fractal dimension by different methods. Obtained values are found to differ from each other, but in general, a larger D_{in} leads to a larger calculated fractal dimension. For subsequent analyses, we use the fractal dimension, D_{box}, estimated by the box-counting method (Panigrahy et al., 2019). Minimal standard deviation can be observed for D_{box}, remaining largely unaffected by the prescribed value of R_t in surface generation. In experiments, the tested rough surface was compressed by a flat silica surface, which was appropriately polished to attain an R_t of 0.101 ± 0.017 μm and R_{rms} of 0.013 ± 0.001 μm, averaged over ten scans of 1×1 mm^2 using a profilometer (Type 1000 WLI, NanoMap).

2.2. Experimental procedures

A schematic of the experimental setup is displayed in Fig. 1 (a). The tested specimen and silica cube block were glued to the bottom and top sample holders, respectively. The relative position of the bottom sample holder can be adjusted horizontally with respect to the fixed base. The top sample holder can move freely along the central axis of the whole device through a high-precision linear guide (LM type, THK Japan), with the radial spacing less than 20 μm. In this case, the contact between the silica block and specimen can be maintained horizontally with a tilt angle of less than approximately 0.001 rad. The entire experimental setup was installed on a rotation stage built into the scanning chamber of a CT scanner (ZEISS Xradia 610). During the test, a constant compression load of 18.33 ± 0.05 N was maintained, which equals the combined gravitational force of the components attached to the top holder, including a dead weight of 1.5 kg, its holder, the linear guide, the top sample holder, and the silica block. At the beginning of each test, the silica block was slowly placed onto the rough specimen and allowed to rest for 30 min. Subsequently, five successive 3DXRCT measurements were conducted at time intervals of 1, 2, 4, and 8 h, with reference to the onset of each CT measurement. During each CT measurement, the entire rough contact was illuminated by an X-ray beam of 80 keV, while the sample was rotated over 360°. The transmitted X-ray radiographs were recorded using an imaging detector with a rotation increment of 0.3°. The recorded transmitted radiographs were used to reconstruct the 3D contact structure. The scanning time for each CT measurement was less than 40 min, and the spatial resolution was approximately 3.0 μm. The power of 3DXRCT enables us to investigate the contact creep of rough

metallic and ceramic surfaces (non-transparent) over a wide temperature range, which is crucial for ensuring safety in many engineering applications and motivates our future research.

2.3. Image processing

We obtained the contact surface evolution by comparing 3D contact configurations realized by successive 3DXRCT measurements. Raw XRCT datasets (Fig. 2 (a)) were processed using a self-developed image analysis algorithm in Matlab©, and the entire process of which is depicted in Fig. 2. Otsu's method (Liu and Yu, 2009) was first employed to globally threshold the images, followed by a local adaptive thresholding procedure based on a 3D window of $7 \times 7 \times 7$ pixels to identify voids and solids (including the silica block and specimen). Binarization was then applied, followed by morphological opening and closing procedures using the same window size to reduce the noise levels. Subsequently, the silica and specimen phases were segmented using the watershed algorithm (Ng et al., 2006), as illustrated in Fig. 2 (e). During the experiments, the specimens were compressed using a flat and smooth silica surface, whose roughness was three orders of magnitude smaller than that of the 3D-printed surfaces. Therefore, the studied contact can be regarded as a deformable rough surface compressed by a rigid flat, with the consideration of the significant differences in mechanical properties of the contact pair. Pixels representing the real contact were identified using a contact search algorithm (Zhai et al., 2019). Based on the watershed algorithm for a two-dimensional (2D) image, individual microcontacts were further segmented, identified, labeled, and tracked during contact creep, as shown in Fig. 2 (e) and (f). The variation of the interfacial separation distance was determined based on the height of the contact surface with respect to the fixed bottom sample holder.

In this study, 3D DVC analysis (Bay et al., 1999); (Taillandier-Thomas et al., 2014) was conducted using SPAM (Stamati et al., 2020) to extract the full-field strains of the entire specimen, including both contact and non-contact zones. We combined the subset-based local DVC and global DVC approaches to accurately resolve the strain field within the contact configuration between two XRCT measurement steps. In the subset-based DVC, the region of interest was divided into smaller sub-volumes, with each sub-volume independently correlated. Although the subset-based local DVC can capture large displacements in less time, its accuracy is reduced owing to the displacement discontinuity at the sub-volume boundaries. Therefore, the local DVC approach can only provide initial estimations of the strain values, and more accurate results can be obtained by further incorporating the global DVC approach. The detailed algorithms for the two types of DVC can be found in Appendix D.

3. Theoretical background

To elucidate the contact evolution, we implemented a concise self-consistent model for the contact of inelastic materials (Storåkers et al., 1997) based on the indentation theory (Oliver and Pharr, 2004) and von Mises isotropic flow theory (Hill, 1948). According to the dimensional similarity analysis and finite element simulations (Storåkers et al., 1997), the microcontact force on a single asperity under normal compression can be considered as a function of the real contact area, material properties, and strain, given by

$$f_i = \alpha \pi r_i^2 E_r (1 + 2N) \left(\frac{\beta r_i}{2R_i} \right)^M \left(\frac{\beta \dot{r}_i \tau_u}{2R_i} \right)^N, \tag{1}$$

where $\alpha = 3$ and $\beta = 1/3$ are universal constants; R_i is the asperity radius; r_i is the contact radius; τ_u is the unit time; and M and N are the hardening and creep exponents, respectively (Larsson et al., 1999). The composite modulus E_r is calculated using $1/E_r = \left(1 - v_1^2\right)/E_1 + \left(1 - v_2^2\right)/E_2$, where E and v are the Young's modulus and Poisson's ratio, respectively, of the material, and the subscripts 1 and 2 indicate the materials of the contacting surface. In the perfectly plastic case, $M = N = 0$ implies no hardening, whereas in the linear case, $M = 1$ and $N = 0$ align with the Hertzian elasticity theory, as displayed in Fig. B1. For a single asperity, we compared the contact and creep behaviors of different materials controlled by the hardening and creep exponents M and N, respectively. The calculated asperity responses were benchmarked with the Hertzian solution and classical elastoplastic model, as detailed in Appendix B.

The overall contact area of the compressed rough surface is collectively contributed by all of its contacting asperities. The decrease in the interfacial separation distance during creep may result in the formation of new microcontacts and merging of the original microcontact areas. To take these effects into consideration, we provided a set of numerical iteration frameworks based on truncation analysis (Zhai et al., 2017); (Zhai et al., 2016). Details of the contact creep calculation of a rough
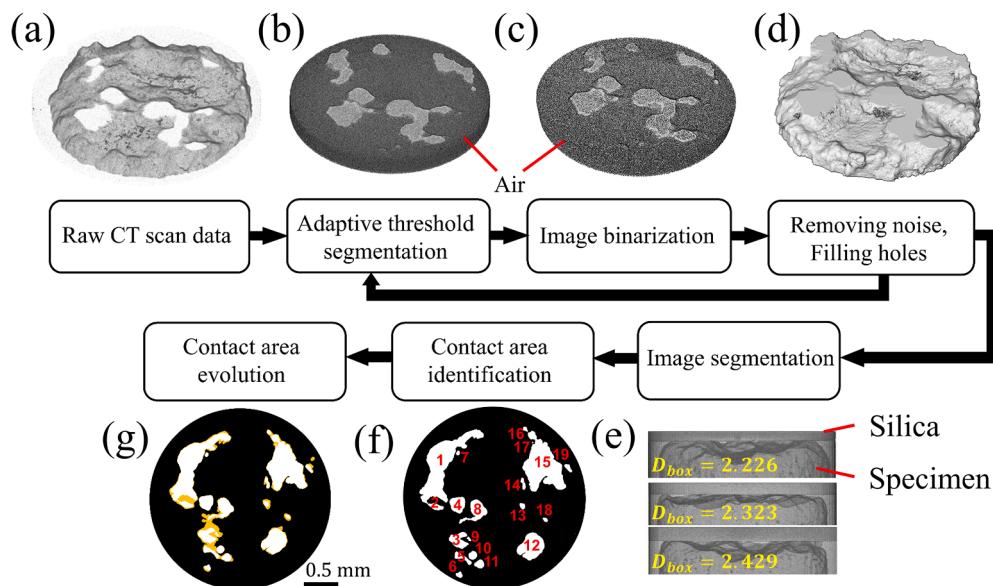

Fig. 2. Flowchart of the image processing. (a) Raw 3DXRCT image of a compressed rough contact. (b) Image thresholding and binarization. (d) Image morphological operations. (e) 3D segmentation of contact interface and silica block. (f) 2D segmentation of microcontacts. (g) Evolution of total contact area over time.

surface under normal compression can be found in Appendix C. In this study, simulations were conducted to thoroughly explore the role of surface structure on contact creep based on the following considerations: (1) isolating the influences of roughness amplitude and fractal dimension, (2) verifying the statistical significance of the experimental observations, and (3) linking observations to their underlying micromechanics.

4. Results and discussion

4.1. Evolution of contact area and interfacial separation distance

For surfaces with various roughness, the total real contact area increases, and the interfacial separation decreases over time during contact creep. The contact area evolution extracted from the XRCT scans for different specimens is depicted in Fig. 3. The increase in the total contact area can be attributed to three mechanisms: merging and expanding of existing microcontacts and formation of new microcontacts. In Fig. 3 (c), the solid line box indicates a typical microcontact merging process, and the dotted circle shows a typical formation process of a new microcontact. During the merging process, a rapid increase in the microcontact area occurs in the early stage, followed by a relatively slow expansion of this area, as illustrated in Fig. 3 (f).

For surfaces with various roughness amplitude and fractal dimensions, we compared the time-dependent contact area and interfacial separation distance, as displayed in Figs. 4 and 5, respectively, extracted from both the experimental observations and numerical simulations. Detailed procedures for numerical simulations are provided in Appendices B (for each asperity) and C (for the overall contact evolution). Numerical results show trends consistent with the experimental observations regarding the influences of roughness amplitude and fractal dimension on the area growth and interfacial separation variation. Overall, for the considered duration, a rougher surface exhibiting the higher fractal dimension and larger roughness amplitude tends to induce a smaller contact area enlargement, as indicated in Fig. 4. A larger variation can be observed in the interfacial separation distance for a surface presenting the smaller fractal dimension and larger roughness amplitude, as illustrated in Fig. 5. Interestingly, contradictory trends are observed for the influence of R_{rms} on the growth of the contact area. On the one hand, R_{rms} is found to be positively correlated with the growth of the contact area in the creep process, as displayed in Fig. 4 (a) and (c), respectively, for experiments and simulations. On the other hand, the negative correlations are observed in Fig. 4 (b) and (d). The fundamental

reason for this phenomenon is that the commonly used parameter, R_{rms}, for characterizing surface roughness can be affected by both the specified R_t and D_{in} in the Weierstrass-Mandelbrot function implemented in this study for generating rough surfaces. Nevertheless, this contradiction indicates that the traditional roughness parameter R_{rms} could be insufficient for properly predicting the contact area enlargement due to creep behavior. Observations shown above support the fact that contact evolution can be strongly influenced by surface roughness, being consistent, in a qualitative manner, with previous studies for natural rough contacts (Gonzalez-Valadez et al., 2010); (Gonzalez-Valadez and Dwyer-Joyce, 2009); (Michalowski et al., 2018) and artificial surface contacts with patterned humps in regular shapes (Pilvelait et al., 2020).

Despite the simplicity of the proposed numerical model, the conducted parametric analyses yield results that exhibit good qualitative agreement with the experimental observations, as depicted in Figs. 4 and 5. Observed disparities between numerical and experimental results may arise from two main assumptions in the proposed model: firstly, the consideration of microcontacts at all contacting asperities as perfectly spherical contacts, disregarding the influence of asperity shapes; and secondly, the absence of interactions between asperities. However, a robust correlation between the microcontact enlargement and asperity shape is evident, as illustrated in Fig. 6. The obtained full-field von Mises strain of the rough surface during the creep process demonstrates the existence of asperity interactions, as detailed in Sec. 4.3. Therefore, factors such as asperity shapes and interactions between asperities are crucial in developing future numerical models for more accurate predictions.

4.2. Influence of microcontact size and asperity shape

In this study, we systematically conducted correlation analyses between the enlargement of the microcontact area and the microcontact structure parameters extracted during the initial measurement step at the onset of contact creep. Here, microcontact area and perimeter are used to describe microcontact size, while considered shape parameters include effective asperity curvature and microcontact aspect ratio. The area and perimeter of a microcontact were calculated based on the number of XRCT pixels belonging to the contact zone and its boundary, respectively. The microcontact aspect ratio is a shape parameter, defined as λ_1/λ_2, where λ_1 and λ_2 are eigenvalues corresponding to the long and short principal axes of the microcontact patch (Zhai et al., 2020). The asperity curvature is another shape parameter calculated by spherical fitting of surficial pixels of the asperity tip, which is assumed to
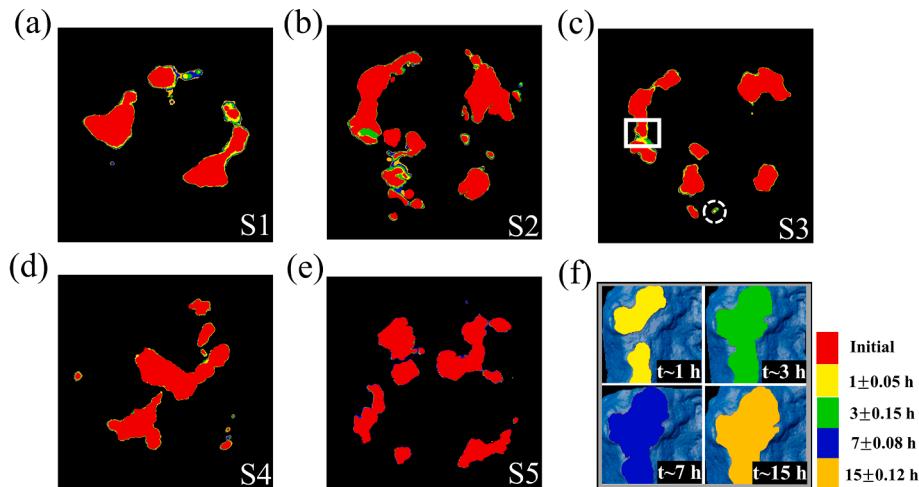

Fig. 3. Contact area evolution captured through successive XRCT measurements: (a)–(e) creep deformation of surfaces for samples S1-S5, respectively; (f) shows the typical microcontact merging process indicated by the solid line box in (c). The typical formation and expansion of a new microcontact are indicated by the long-dotted circle in (c). Colors indicate the microcontacts obtained at different measurement steps.
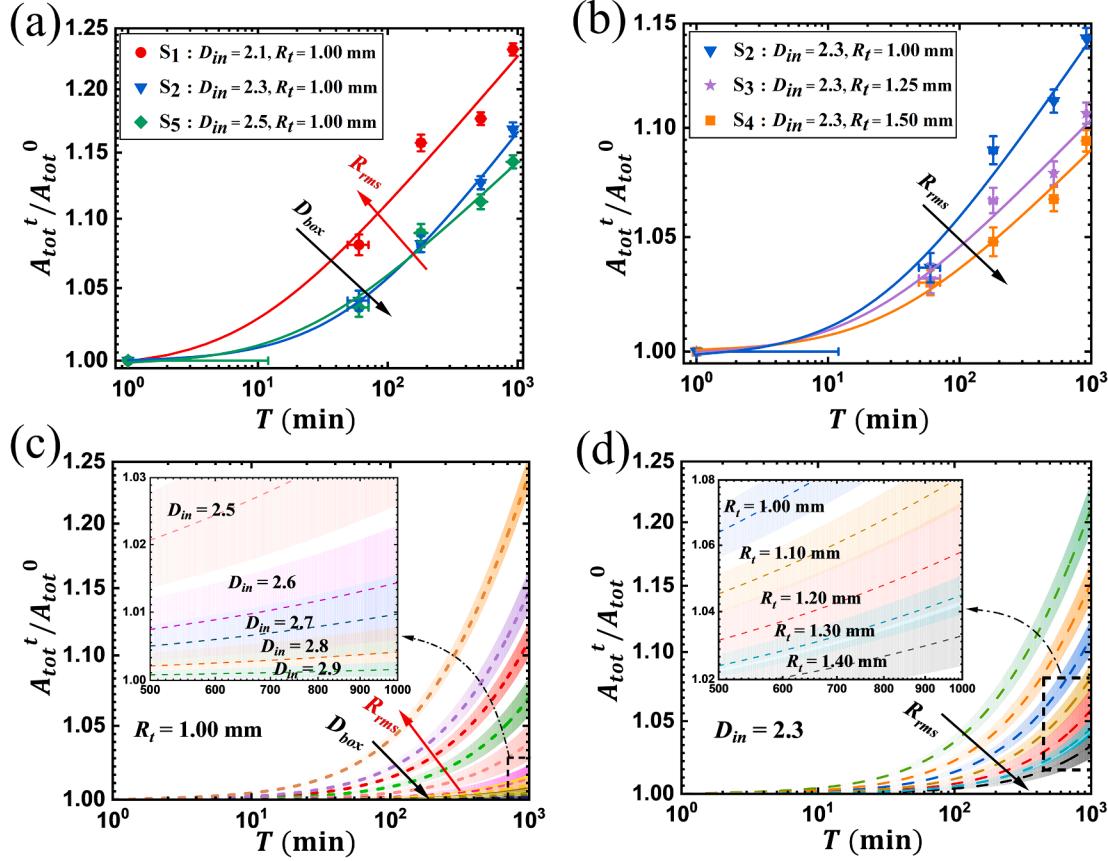
Fig. 4. Contact area evolution for surfaces with various roughness: (a) experimental measurements for 3D-printed sample surfaces, including S1, S2, and S5, exhibiting the identical roughness amplitude R_t and varying D_{in}; (b) experimental measurements for 3D-printed surfaces, including S2, S3, and S4, with identical D_{in} and various R_t; (c) provides numerical results for surfaces with identical prescribed roughness amplitude, i.e., $R_t = 1.0$ mm, and various D_{in} ranging from 2.1 to 2.9 with an increment of 0.1. (d) shows numerical results for surfaces with the same prescribed fractal dimension values, i.e., $D_{in} = 2.3$, and varying roughness amplitude R_t ranging from 0.8 mm to 1.4 mm with an increment of 0.1 mm. The measured and estimated total contact area, A_{tot}^t, are normalized by the initial total area, A_{tot}^0. Solid lines in (a) and (b) are corresponding fitting curves. The shaded areas in (c) and (d) indicate the standard deviation calculated over ten realizations. Inserts in (c) and (d) are enlarged views for zones in dashed squares.

be ideally spherical. Considering the XRCT resolution (<3 μm) and complex shapes of large microcontacts, only microcontacts greater than 10 % and smaller than 90 % of the largest microcontact were included in conducted correlation analyses. To reasonably merge datasets from different measurement steps and across all samples, the data collected for a specimen at a given measurement step was normalized with the standard score, that is, $S_c(X_i) = (X_i - \langle X \rangle)/std(X)$. Here, X represents the dataset, while $\langle X \rangle$ and $std(X)$ are, respectively, the mean and standard deviation values. As illustrated in Fig. 6, the growth of the microcontact area is found to be positively correlated with microcontact size parameters, including the microcontact area (Fig. 6 (a)) and perimeter (Fig. 6 (c)). In contrast, the microcontact enlargement is found to be negatively correlated with the asperity curvature (Fig. 6 (b)). The correlation coefficient of less than 0.1 indicates that the microcontact aspect ratio tends to play an insignificant role in microcontact creep. The significantly higher correlation coefficients observed for size parameters (0.77 and 0.76, respectively, for the microcontact area and perimeter) than those of shape parameters (0.55 and 0.08 for the asperity curvature and microcontact aspect ratio, respectively) indicate that the microcontact size tends to have a more important role than the asperity shape.

The aforementioned correlation analyses based on the experiments are supported by the micromechanical model that is detailed in Appendices B and C. While achieving only qualitative rather than quantitative agreement between the experiments and analytical solutions, this approach aids in elucidating the fundamental mechanisms underlying experimental observations. For a single asperity, the rela-

tionship between the growth of the contact area and its radius can be deduced from Eq. (B2) with further simplification:

$$a_i(t) \sim R_i^2 \left[\left(\frac{f_i}{E_r R_i^2} \right)^{\frac{1}{N}} \left(\frac{t}{\tau_u} \right) \right]^{\frac{2N}{M+N+2}}. \tag{2}$$

Here, the eliminated term in the series expansion $\left(\frac{a_i(0)}{\pi R_i^2} \right)^{\frac{M+N+2}{2N}}$ is considered to be responsible for the contact status at the onset of creep. The scaling relationship can then be given between the microcontact area growth and asperity curvature, that is, $\dot{a}_i(t) \propto \kappa_i^{\alpha_\kappa}$, where κ_i is the curvature, $\kappa_i = 1/R_i$, and the exponent α_κ can be roughly estimated as $-\frac{2(M+N)}{M+N+2} = -0.68$. The exponent extracted from the curve fitting using the experimental data displayed in Fig. 6 (b) is approximately 0.69. By substituting $f_i \propto a_i(0)^{1+\frac{M}{2}}$ deduced from Eq. (B1) into Eq. (2), a similar relationship for a_i can be obtained, that is, $\dot{a}_i(t) \propto a_i^{\alpha_a}$, where $\alpha_a \approx 2(1 + M/2)/(M + N + 2) = 0.91$. The exponent of α_a obtained by the slopes of the linear fitting curves using the experimental data in Fig. 3 (a) is approximately 0.75. The absolute values obtained from the experimental data fitting are similar to those of the estimated α_a and α_κ using Eq. (2). Although not sufficiently rigorous in simplifying the nonlinearity in contact behavior, these simple scaling analyses provide valuable insights for interpreting the interface morphological dependence of the contact area evolution on fractal rough surfaces. Note that the materials used in this study are a typical synthetic polymer for additive manufacturing, whose mechanical properties, including strength,
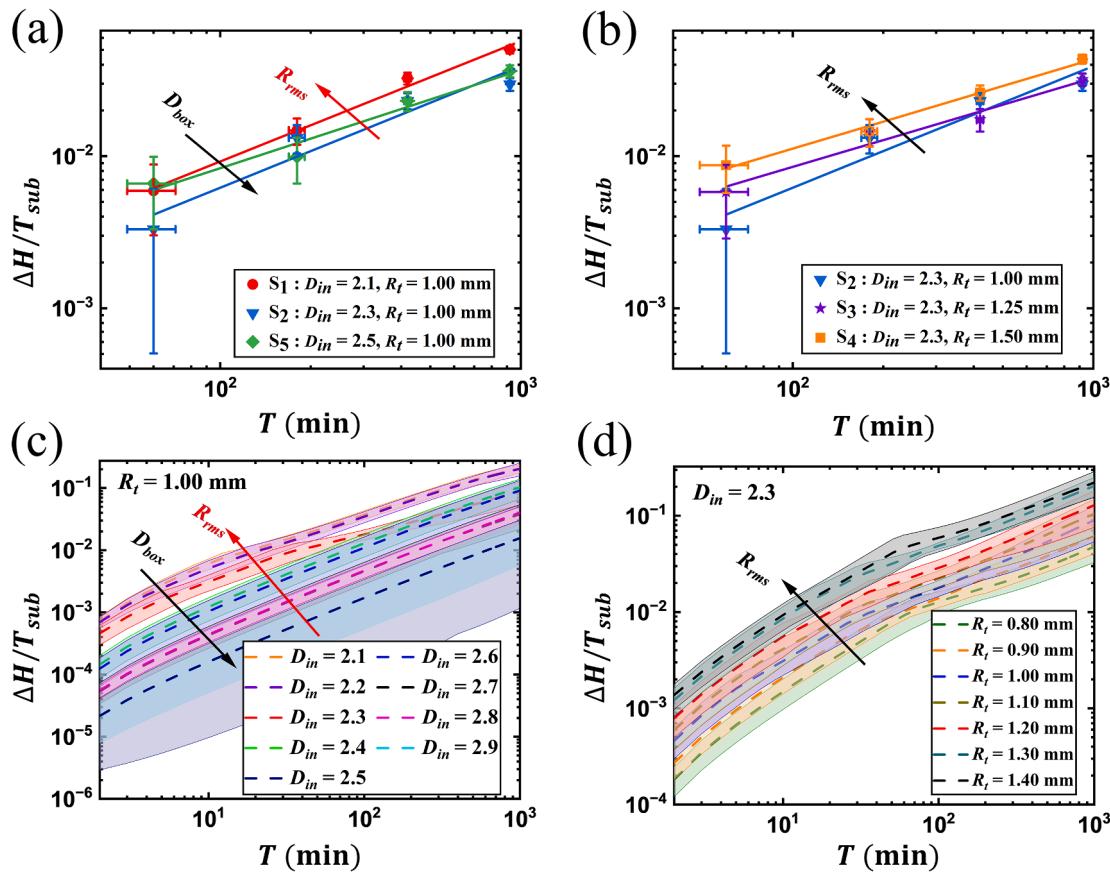
Fig. 5. Variation of interfacial separation during contact creep for surfaces with various roughness: (a) experimental measurements for 3D-printed sample surfaces, including S1, S2, and S5, exhibiting the identical roughness amplitude R_t and varying D_{in}; (b) experimental measurements for 3D-printed surfaces, including S2, S3, and S4, with identical D_{in} and various R_t; (c) provides numerical results for surfaces with identical prescribed roughness amplitude, i.e., $R_t = 1.0$ mm, and various D_{in} ranging from 2.1 to 2.9 with an increment of 0.1. (d) shows numerical results for surfaces with the same prescribed fractal dimension values, i.e., $D_{in} = 2.3$, and varying roughness amplitude R_t ranging from 0.8 mm to 1.4 mm with an increment of 0.1 mm. The measured and estimated variations of the interfacial separation distance, ΔH, are normalized by the surface substrate size $T_{sub} = 0.5$ mm. Solid lines in (a) and (b) are corresponding fitting curves. The shaded areas in (c) and (d) indicate the standard deviation calculated over ten realizations.

module, and viscoelasticity are significantly different from those of alloys, ceramics, wood, etc. Nevertheless, obtained theoretical analyses and numerical results based on the implemented inelastic contact model (Larsson et al., 1999); (Olsson and Larsson, 2013); (Storåkers et al., 1997) are consistent with experimental observations in terms of time-dependent macroscopic responses shown in Figs. 4 and 5, and the creep behavior of individual asperity shown in Fig. 6. The variations of contact creep responses for different materials are primarily controlled by values of M and N in Eq. (1). To show the quantitative differences across materials, we compare asperity responses for different values of hardening and creep exponents, i.e., M and N, respectively, in Appendix B. Results show that materials with a lower creep exponent, such as ceramics, tend to creep slower, and the influence of roughness on contact creep tend to maintain in a qualitative way.

4.3. Mapping of full-field von Mises strain

The contact creep affecting the microcontact area and height ultimately changes the strain/stress status at the contact interface, which is crucial for predicting material damage and structural failure. In this study, we conducted a 3D DVC analysis to calculate the strain evolution during the creep contact process. In the DVC analysis, the accessible 3D contact structure included a compressed specimen of the rough surface, a portion (approximately 30 slices) of the top sample holder, and a portion (30 slices) of the bottom sample holder, which was considered fixed during the experiment. The contact configuration obtained in the

first 3DXRCT measurement step was used as the reference structure from which the evolution of the entire contact structure in the subsequent measurement steps could be readily quantified. For simplicity, we denoted the contact deformation of the n-th step with respect to the first measurement step as dn-1. Using DVC, the pixel-wise von Mises strain (ε) of the entire contact structure was calculated as $\sqrt{6}/3\sqrt{e : e}$ in Cartesian coordinates, where e is the deviant strain tensor of each pixel. The DVC analysis was performed using a window voxel size of $5 \times 5 \times 5$. Notably, the information of the physical contact interface was constrained by only one layer of voxel and thus, the calculation of the gradient at the contact interface was difficult. The chosen DVC voxel with a specific size (used to calculate strain) containing the real contact interface was subtle, because averaging the strain in the whole voxel-window would underestimate the contact strain, especially for asperities with larger surficial gradients. Therefore, we focused on the lower part of the DVC voxels when computing the strain, using approximately five voxels below the macrocontact interface. Surfaces with various D_{in} and R_t are illustrated in Figs. 7 and 8, respectively.

The pixel-wise strain scatters over a wide range, with high strains commonly occurring at the asperity tips. Large strains, for example, $\varepsilon > 0.2$, can be observed in both the contacting and non-contacting zones. Asperity interactions can be tentatively located by large strains observed in those saddle-shaped structures formed between two adjacent contacting asperities, which can be seen in Figs, 7 and 8. Specimen S4 exhibits the highest R_{rms}, demonstrates the largest strain among all specimens during the contact creep process. Previous studies (Yastrebov
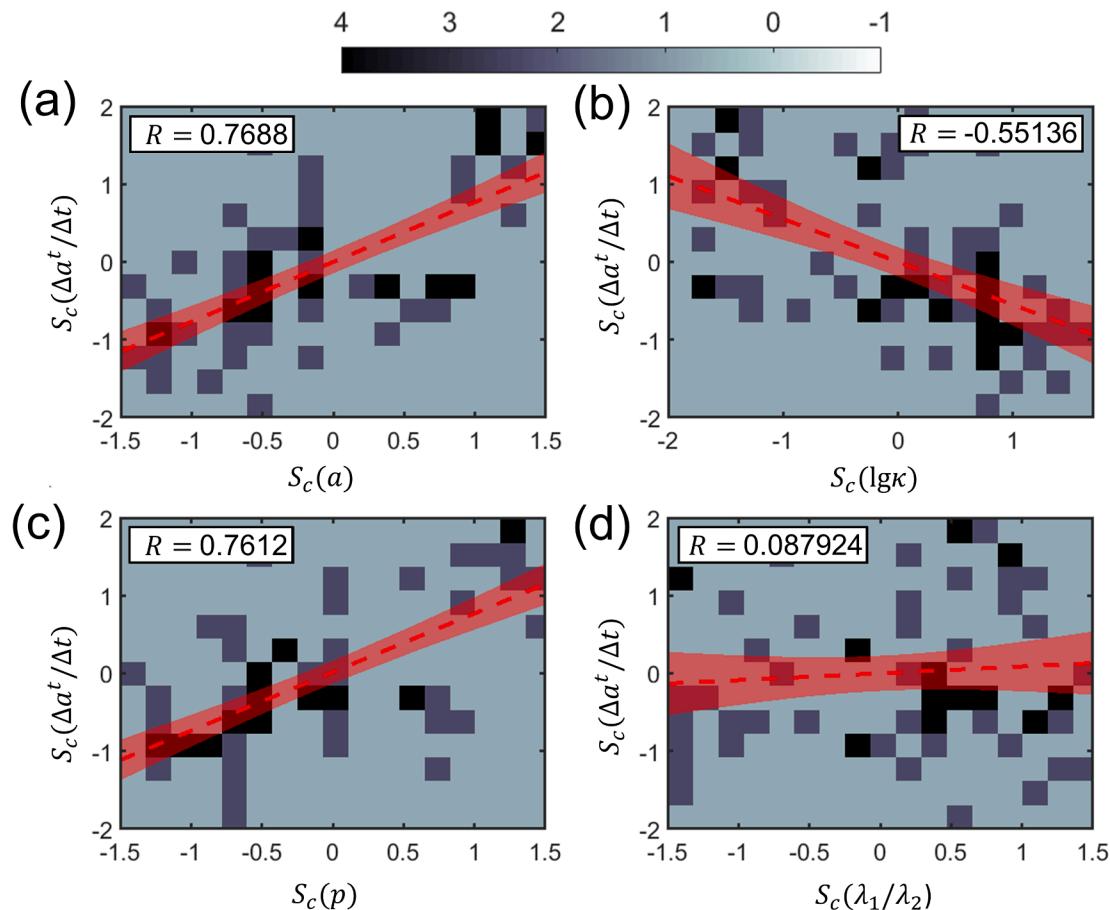
Fig. 6. Correlation analysis between the growth of microcontact area and microstructure parameters. Size parameters include (a) microcontact area and (c) microcontact perimeter; Shape parameters include (b) asperity curvature and (d) microcontact aspect ratio. Joint probability distributions are presented and the shaded area in red represents the 95% confidence interval, while the dotted line in red is the linear fitting curve.
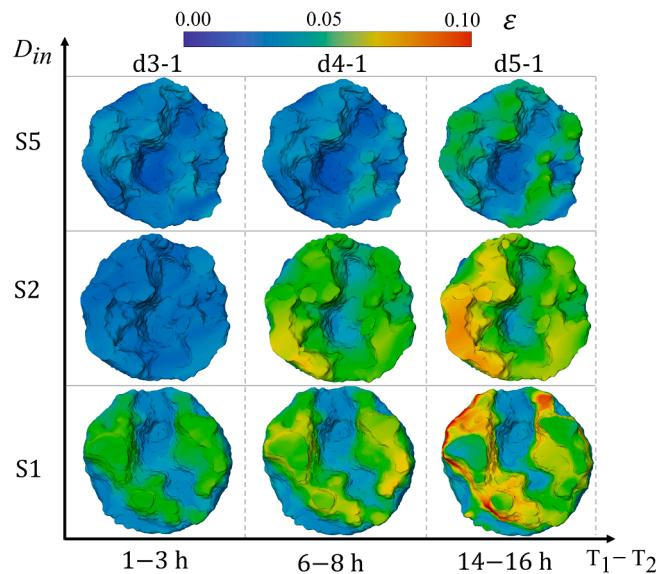

Fig. 7. The evolution of von Mises strains for surfaces with a constant roughness amplitude (R_t) and varying fractal dimension (D_{in}).

Fig. 8. The evolution of von Mises strains for surfaces with a constant fractal dimension (D_{in}) and varying roughness amplitude (R_t).

et al., 2015); (Zhai et al., 2017) have suggested that under a fixed compression load, a rougher surface tends to present a smaller contact area with a relatively higher contact pressure unevenly distributed over microcontacts. Intuitively, this initially higher contact pressure at the
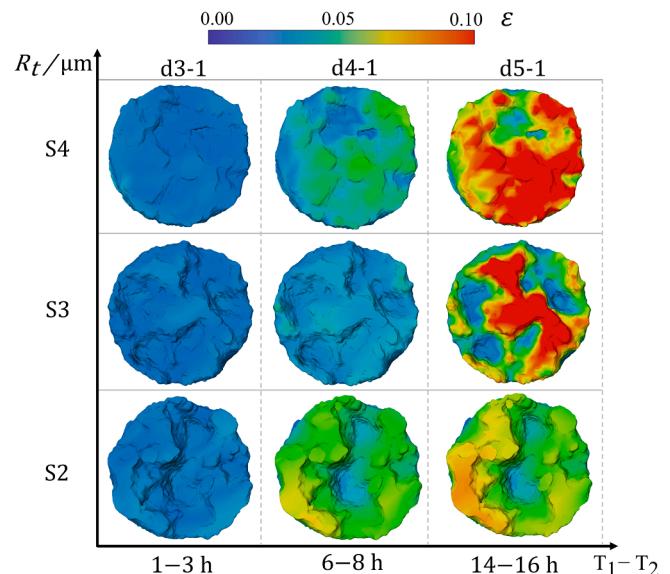
onset of contact creep for a rougher surface can potentially accelerate the creep process, as supported by the positive correlation between the microcontact force and growth of the microcontact area, which is suggested in Eq. (B2) of Appendix B. However, both our experimental and

numerical results reveal that the contact areas of rougher surfaces with higher values of R_t expand less but deform more in non-contacting zones. The observed large strains in non-contacting zones motivate us to investigate the structure evolution at non-contacting zones. Two typical non-contacting regions are selected: case (1) for the region near an isolated asperity, and case (2) for the saddle-shaped region between two interacting asperities. To describe surface geometrical features at the non-contacting zones, we quantified the local horizontal curvature and surface gradient denoted by κ_{xy} and g_{surf}, respectively. For calculating κ_{xy} of each surficial pixel, an edge detection algorithm (Rong et al., 2014) was first used to extract a set of surface contours from the surface bottom to the height of five slices (approximately 18 μm) away from the contacting height. Subsequently, the horizontal local curvature of each pixel on the contour was calculated by circle fitting for a given pixel together with the nearest eight pixels on the contour. A positive (negative) value of the curvature indicates the degree of convexity (concavity). The amplitude of the gradient at surficial pixels, indicating the local inclination was obtained using the Canny-Deriche algorithms (Sangeetha and Deepa, 2019). For the region near the isolated asperity, i.e., case (1), circled in Fig. 9 (a), distributions of roughness features including pixel-wise κ_{xy} and g_{surf} are found to vary slightly across measurement steps, whereas obvious variations in κ_{xy} and g_{surf} can be observed within the region between interacting asperities, i.e., case (2), as depicted in Fig. 9 (d). This distinction suggests that one effect of asperity interactions is to alternate the local roughness structures. This information has usually been ignored in previous analytical solutions for rough contacts by assuming that the geometries at non-contacting zones remain unchanged during the loading process, which might be an important reason why qualitative rather than quantitative agreement can be achieved in our asperity-based model. We further performed correlation analysis between contact strain and roughness parameters, including κ_{xy} and g_{surf}, as detailed in Appendix E. Consistent correlation trends observed across samples and load steps support that local deformation and roughness features at non-contacting zones cannot be mutually exclusive during the creep process.

This study showed that rough surfaces under constant normal compression at room temperature can experience significant creep deformation, exhibiting simultaneous variations in the contact area and interfacial separation distance. The enlargement of the contact area and decrease in the interfacial separation distance are closely associated during the creep process, where asperities interact through deformation in non-contacting zones to redistribute the contact pressure and adjust the interfacial gap. The contact evolution resulting from the expansion of existing microcontacts and the formation of new microcontacts is influenced by the creep behavior of asperities in both the contacting and non-contacting zones. Existing studies rely heavily on the evolution of the contact area to predict interfacial behavior, such as contact stiffness, adhesion, and electrical and thermal contact conduction (Ciavarella et al., 2019); (Komvopoulos, 2020); (Wang et al., 2021); (Zhai et al., 2016). However, research on the evolution of non-contacting zones at interfaces is limited. These zones can deform significantly owing to strong asperity interactions, potentially affecting the global interfacial behavior (Jeng and Peng, 2006); (Li et al., 2018); (Wang et al., 2017); (Yeo et al., 2010), such as sealing, surface wear, and contact creep reported in this study, which is a noteworthy aspect that deserves special attention.

5. Summary and conclusion

We presented our experimental setup and data processing techniques for studying the contact creep phenomenon. The influence of surface roughness on contact creep under constant normal compression was systematically investigated using 3D printing and 3DXRCT measurements. A series of 3D-printed specimens with rough surfaces exhibiting various D_{box} and R_t values were examined. To elucidate the interfacial
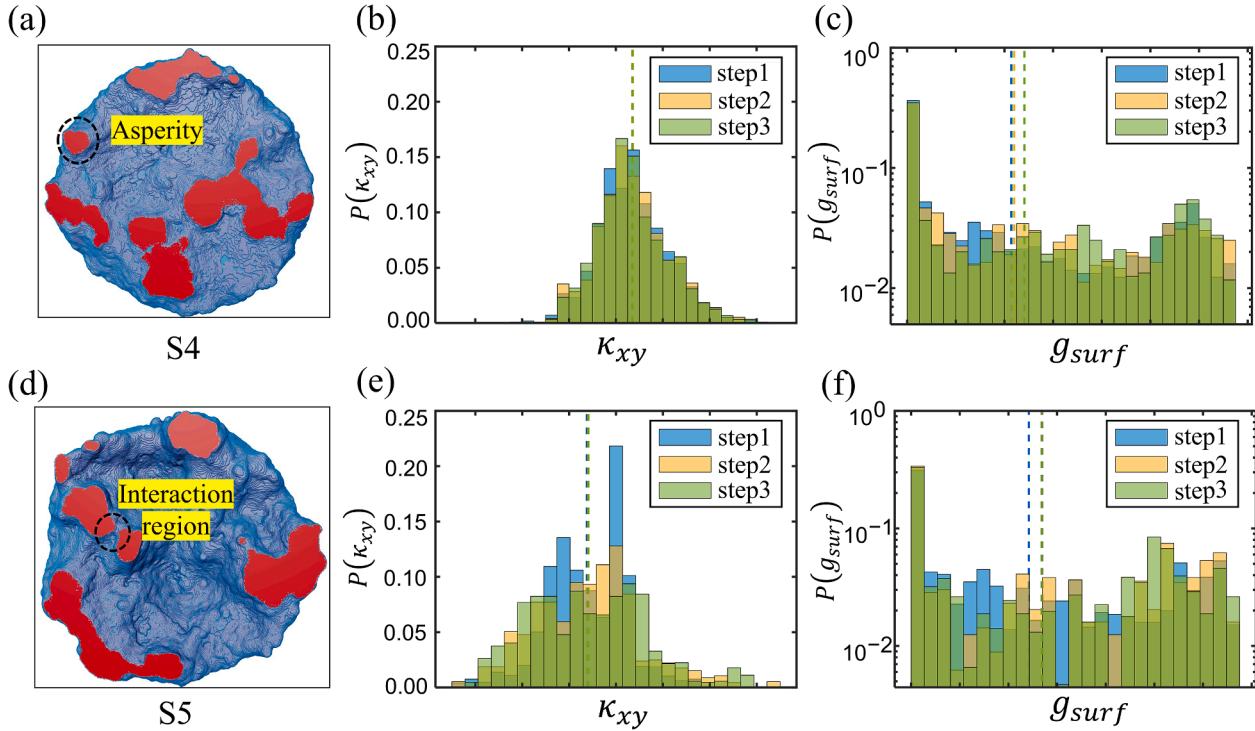

Fig. 9. Structural evolutions at typical non-contacting regions during the creep process. The circle in (a) highlights the region close to an isolated asperity. The circle in (d) indicates the region between two interacting asperities. Values of κ_{xy} and g_{surf} are extracted for surficial pixels within the cylindrical regions of approximately 120 μm in diameter and 20 μm in height, defined by the two circles in (c) and (f). The probability distributions of κ_{xy} and g_{surf} given in (b) and (c) are extracted in the cylindrical region shown in (a). The probability distributions of κ_{xy} and g_{surf} given in (e) and (f) correspond to the cylindrical region in (d). Vertical dashed lines indicate the respective mean values of κ_{xy} and g_{surf} for the first, third, and fifth measurement steps, denoted by step1, step3, and step5.

micromechanics, deformations during the creep process in both contacting and non-contacting zones were investigated using DVC analysis. Through comparison between experimental observations and qualitative numerical predictions, together with parametric analysis, the following conclusions were drawn: (1) Surface roughness can significantly influence both contact area enlargement and variation of interfacial separation distance. The former is found to decrease with roughness amplitude and fractal dimension, while the latter increases with roughness amplitude and decreases with fractal dimension. (2) The microcontact size plays a more significant role than the shape in determining the enlargement of the microcontact area. (3) At the non-contacting zones, the roughness structure and local deformation mutually influence each other, and this influence can be enhanced by asperity interactions.

CRediT authorship contribution statement

Shaoqi Huang: Formal analysis, Data curation, Investigation, Methodology, Validation, Visualization, Writing – original draft, Writing – review & editing. **Deheng Wei:** Conceptualization, Data curation, Formal analysis, Investigation, Methodology, Software, Validation, Writing – original draft, Writing – review & editing. **Wenwen Han:** Data curation, Investigation, Software, Validation, Writing – review & editing. **Hengxu Song:** Conceptualization, Investigation, Writing – review & editing. **Siyang Song:** Writing – review & editing, Data curation, Investigation, Methodology. **Yixiang Gan:** Writing – review & editing, Supervision, Conceptualization. **Chongpu Zhai:** Writing – review & editing, Writing – original draft, Visualization, Validation, Supervision, Software, Resources, Project administration, Methodology, Investigation, Funding acquisition, Formal analysis, Data curation, Conceptualization. **Minglong Xu:** Writing – review & editing, Supervision, Resources, Project administration, Investigation, Conceptualization.

Declaration of competing interest

The authors declare that they have no known competing financial interests or personal relationships that could have appeared to influence the work reported in this paper.

Data availability

Data will be made available on request.

Appendix A

Surface generation and characterization

The height function $z(x,y)$ of a three-dimensional isotropic rough surface can be simulated by the modified Weierstrass-Mandelbrot function (Komvopoulos, 2020), i.e.,

$$z(x,y) = L\left(\frac{G}{L}\right)^{(D_{in}-2)}\left(\frac{ln\gamma}{M}\right)^{\frac{1}{2}}\sum_{m=1}^{M}\sum_{n=0}^{n_{max}}\gamma^{(D_{in}-3)n}\#$$

$$\times\left\{cos\phi_{m,n} - cos\left[\frac{2\pi\gamma^n(x^2+y^2)^{\frac{1}{2}}}{L}cos\left(tan^{-1}\left(\frac{y}{x}\right) - \frac{\pi m}{M}\right) + \phi_{m,n}\right]\right\},$$

$$(A1)$$

where L is the length of the imaged surface profile, G is the fractal roughness, which is related to the roughness amplitude R_t ($G = L\left[R_t/L \times (M/ln\gamma)^{0.5}\right]^{1/(D_{in}-2)}$). Here, D_{in} is the prescribed fractal dimension. The value γ determines the density of frequencies to construct the surface profile, which is set here as 1.5 after considering surface flatness and frequency distribution density. The scaling parameter γ plays another important role in the fractal description. Specifically, if the lateral length x is magnified by γ, then the height z is magnified by $\gamma^{(3-D_{in})}$. The factor M is the number of superposed ridges that are used to construct the surface profiles, n_{max} represents the top bound of the frequency index that can be determined by ($n_{max} = int[log(L/L_s)/log\gamma]$), where $int[\dots]$ denotes rounding off of the quantity enclosed within the brackets to its maximum integer and L_s is the smallest wavelength in the surface profile. The minimum value of L_s should be limited to 5–6 times the material lattice distance. The parameter $\phi_{m,n}$ is a set of randomly distributed phase angles to ensure randomness. In addition to the above necessary parameters, a rough surface is often characterized by root-mean-square roughness R_{rms}, i.e

$$R_{rms} = \sqrt{\frac{1}{L^2}\int_0^L\int_0^L|z(x,y)|^2\mathrm{d}x\mathrm{d}y}.$$

$$(A2)$$

It should be noted that the fractal dimension of rough surfaces can be evaluated using different methods, including the vertical sections method (Klinkenberg and Goodchild, 1992), power spectrum analysis (Talebinejad et al., 2009), triangulation method (De Santis et al., 1997), and box-counting method (Li et al., 2009), etc. With different methods, the evaluated value of fractal dimension can be largely different, for a given surface, as is demonstrated in the literature (Chen et al., 2018); (Dubuc et al., 1989); (Gallant et al., 1994) and our previous studies (Zhai et al., 2017); (Zhai et al., 2023). In this study, we prescribe the fractal dimension, D_{in}, ranging from 2.1 to 2.5 in Eq. (A1) of current Appendix A. The actual surface fractal dimension for the 3D printed samples is estimated by the box-counting method and the D_{box} ranging from 2.23 to 2.43, which is slightly different from the prescribed fractal dimension, D_{in}. For comparison, we provide in Table A1 values of fractal dimension calculated based on different methods. Values based on the power spectra are found to range from 2.06 to 2.22, consistent with (Persson, 2014).

Table A1

Comparison between the input fractal dimension and the characteristic fractal dimension calculated by different methods for rough surfaces, i.e., the box-counting method D_{box}, the power spectral method D_{sp}, and the fractional Brownian motion method D_{fbm} (Liu et al., 2014).

D_{in}	D_{box}	D_{sp}	D_{fbm}
2.1	2.226 ± 0.008	2.065 ± 0.041	2.485 ± 0.005
2.2	2.264 ± 0.014	2.091 ± 0.044	2.526 ± 0.009
2.3	2.324 ± 0.008	2.141 ± 0.037	2.577 ± 0.005
2.4	2.363 ± 0.009	2.177 ± 0.022	2.624 ± 0.005
2.5	2.429 ± 0.006	2.225 ± 0.014	2.679 ± 0.003
2.6	2.484 ± 0.007	2.237 ± 0.009	2.742 ± 0.002
2.7	2.542 ± 0.005	2.257 ± 0.005	2.795 ± 0.003
2.8	2.595 ± 0.011	2.331 ± 0.004	2.845 ± 0.002
2.9	2.648 ± 0.010	2.414 ± 0.003	2.890 ± 0.002

In this study, the unrecoverable sample height after testing further demonstrates that linear elasticity cannot work for considered rough surfaces. After removing the normal compression load of 25 N, the sample height has been found to shirk up to 145 μm with respect to the initial height, as is listed in Table A2. After removing small compressions applied, i.e., 3 N, the tested surfaces can almost recover to the initial height, where the elastic behavior dominates the mechanical responses. However, significant differences of up to 15 % can be observed between H^1 and H^2, indicating significant unrecoverable surface modifications.

Table A2

Variations of sample height.

Sample	H^0/ mm(Initial height)	H^1/ mm (Removing compression, 1 MPa)	H^2/ mm (Removing compression, 8 MPa)
S1	1.00	0.992 ± 0.0023	0.855 ± 0.0286
S2	1.00	0.992 ± 0.0029	0.858 ± 0.0185
S3	1.25	1.242 ± 0.0025	1.105 ± 0.0298
S4	1.50	1.496 ± 0.00045	1.354 ± 0.0205
S5	1.00	0.990 ± 0.00063	0.901 ± 0.0238

Note: compressive stress is calculated by F_n/A_a, where F_n is the normal compression load and A_a is the apparent area.

Appendix B

Contact behavior of a single asperity under normal compression

For a spherical asperity, it is reasonable to assume that the asperity curvature, $1/R_i$, is constant, due to the small contact inference (Ghaednia et al., 2016). By substituting $r_i(t) = \sqrt{a_i(t/\tau_u)/\pi}$ into Eq.(1), the relationship between time-dependent microcontact load, $f_i(t)$, and microcontact area, $a_i(t)$, can be expressed as:

$$f_i(t) = \frac{\alpha\pi(1+2N)(\beta)^{M+N}(E_r R_i^2)}{2^{M+2N}}\left(\frac{a_i(t/\tau_u)}{\pi R_i^2}\right)^{\frac{(M-N+2)}{2}}\left[\frac{\mathrm{d}}{\mathrm{d}t}\left(\frac{a_i(t/\tau_u)}{\pi R_i^2}\right)\right]^N, \# \tag{B1}$$

where $a_i(t/\tau_u)$ is the microcontact area evolving with the normalized time. Moreover, the evolution of an individual microcontact area under constant load can be then obtained by integrating Eq. (B1).

$$a_i(t) = \pi R_i^2\left\{\frac{M+N+2}{N}\left[\frac{f_i/(E_r R_i^2)}{\alpha\pi(1+2N)(\beta/2)^{M+N}}\right]^{\frac{1}{N}}(t/\tau_u) + \left(\frac{a_i(0)}{\pi R_i^2}\right)^{\frac{M+N+2}{2N}}\right\}^{\frac{2N}{M+N+2}}, \# \tag{B2}$$

where $a_i(0)$ is the initial microcontact area. Eq. (B2) shows that the contact area and time show a quasi-linear relationship in the log–log scale, and are controlled by the normal load, radius of asperity curvature, initial microcontact area, and material properties.

In Fig. B1, we show the growth of the real contact area for a single asperity under a constant normal load. We compute the asperity responses with various values of *M* and *N*, representing different types of materials, benchmarked with results calculated by the Hertzian solution and elastoplastic model (Zhao and Chang, 2001), as shown in Fig. B1. In the perfectly plastic case, $M = N = 0$ implying no hardening, while in the linear case, $M = 1$, $N = 0$ harmonizing with Hertzian elasticity theory. The value of *N* is found to significantly influence the asperity creep.
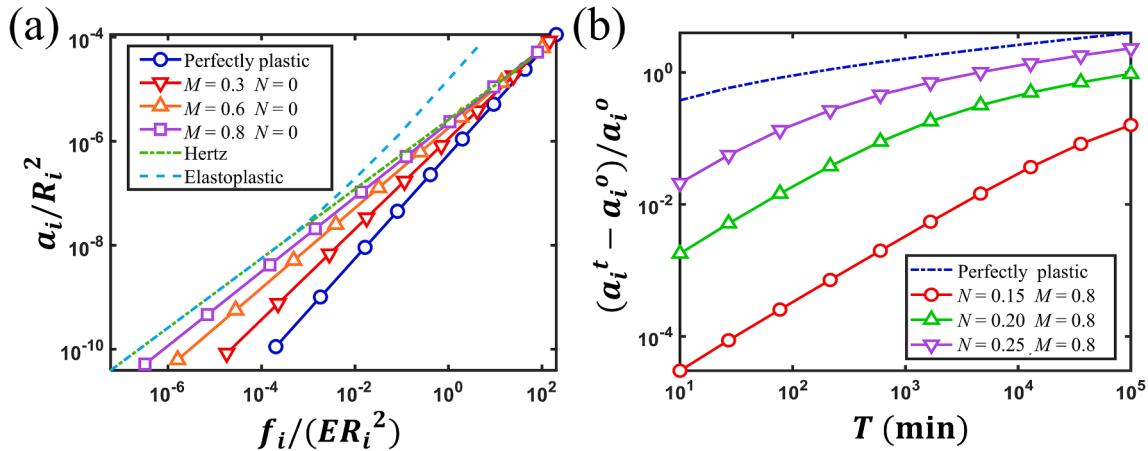
Fig. B1. Contact responses of a single asperity under normal compression. (a) The relationship between dimensionless load and contact area for different hardening exponents. The circle marker indicates the case of perfect plasticity. The upper triangle, lower triangle and square indicate cases of various hardening materials. The short and long dashed lines indicate results for classic Hertzian solution and elastoplastic model (Zhao & Chang, 2001). (b) The variation of real contact area with time under a constant load. Here, the dotted line indicates the case of perfectly plastic with and . Markers of circle, upper and lower triangles are for cases of different creep exponents.

Appendix C

Numerical framework for determining contact creep

The contact creep of a rough surface under the constant normal load would generally cause the decrease of interfacial separation distance over a specified duration. Consequently, the variation of the contact is accompanied by the formation of new microcontacts and the merging of the original microcontact areas, leading to the continuously varying contact area and the distribution of contact pressure. To elucidate the contact enlargement and the decrease of interfacial separation distance happening simultaneously during the contact creep, we proposed a comprehensive numerical framework based on the contact behavior of a single asperity under normal compression, as discussed in Sec. 3. Three iterations of contact inference are implemented, as shown in the flow chart of Fig. C1. The first iteration ensures that the overall reaction force collected from all contacting asperities equals the preset normal load (Zhai et al., 2017); (Zhai et al., 2023), at the onset of the creep process. The second iteration is to obtain the creep deformation of the whole contact surface with respect to time. The third iteration is embedded into the second iteration to calculate the incremental creep deformation while maintaining the constant normal load.

For the overall the decrease of interfacial separation distance caused by creep, Δh, the variation of microcontact area is contributed by different mechanisms, including newly forming, merging, and expanding. Considering the fractality nature of the compressed rough surface, the contact deformation of the maximum microcontact plays an essential role in controlling the overall contact deformation. Therefore, we associate the incremental interfacial separation distance, Δh, with the contact inference of the maximum microcontact, $\Delta \delta_{max}$, $\Delta h = K^{num} \times \Delta \delta_{max}$, at time step $t + \Delta t$. Here, K^{num} is a correction factor with an initial value of one, $\Delta \delta_{max}$ can be approximated by geometric conditions for spherical asperity due to small deformation, i.e., $\Delta \delta_{max} = \Delta a_{max}/(2\pi R_{max})$, where Δa_{max} represents the maximum microcontact area increment in a time step, $\Delta a_{max} = a_{max}(t+\Delta t) - a_{max}(t)$, and $a_{max}(t+\Delta t)$ is calculated by

$$a_i(t + \Delta t) = a_i(t) + 2\pi R_i^2 \left[\frac{f_i(t)/(E_r R_i^2)}{\alpha\pi(1 + 2N)(\beta/2)^{M+N}} \right]^{\frac{1}{N}} \left[\frac{a_i(t)}{\pi R_i^2} \right]^{-\frac{M-N+2}{2N}} \Delta t. \# \tag{C1}$$

The determination of the optimal value of K^{num} through the third iterative process is essentially controlled by the equilibrium condition of forces, i. e., $\sum_i f_i^{t+\Delta t} = F_n$. Here, Eq. (C1) is obtained by reorganizing Eq. (B2) but expressed in differential form. Noticeably, Eq. (C1) is used to calculate the growth of the maximum microcontact area in the third iteration, thus being capable of determining the value of K^{num} and the decrease of interfacial separation distance at time step $t + \Delta t$. With this estimated decrease of interfacial separation distance, the variations of all microcontacts are then estimated by truncation analyses. The total load can be calculated by summing all the microcontact forces, i.e., $F_{tot}^{t+\Delta t} = \sum_i f_i^{t+\Delta t}$, and contact area is calculated by $A_{tot}^{t+\Delta t} = \sum_i a_i^{t+\Delta t}$. Different deformation states of microcontact are also considered, depending on the critical truncation area, i.e., a_i^c, critical area indicating the transition from elastic to elastoplastic behavior . In the elastic regime, we set $M = 1$, $N = 0$, $M = 0.8$, $N = 0.25$ for the elastoplastic regime, and $M = 0$, $N = 0.25$ for the full plastic regime. Additionally, the implemented numerical approach for estimating interfacial electro-mechanical behavior can be affected by the spatial resolution of simulated surfaces and increment steps of truncation depth. To achieve satisfactory convergence of numerical results, 8096 × 8096 pixels over the area of 2.5 mm × 2.5 mm are selected to ensure numerical convergence (Zhai et al., 2017); (Zhai et al., 2023). The incremental truncation depth Δh of less than 1 μm is used, which is significantly smaller than the smallest roughness feature of 3D-printed specimens. The temporal resolution in conducted iterations is 1 min. Results show ignorable differences in the contact area and contact displacement with higher spatial resolutions of simulated surfaces, finer truncation increments, and higher temporal resolution.
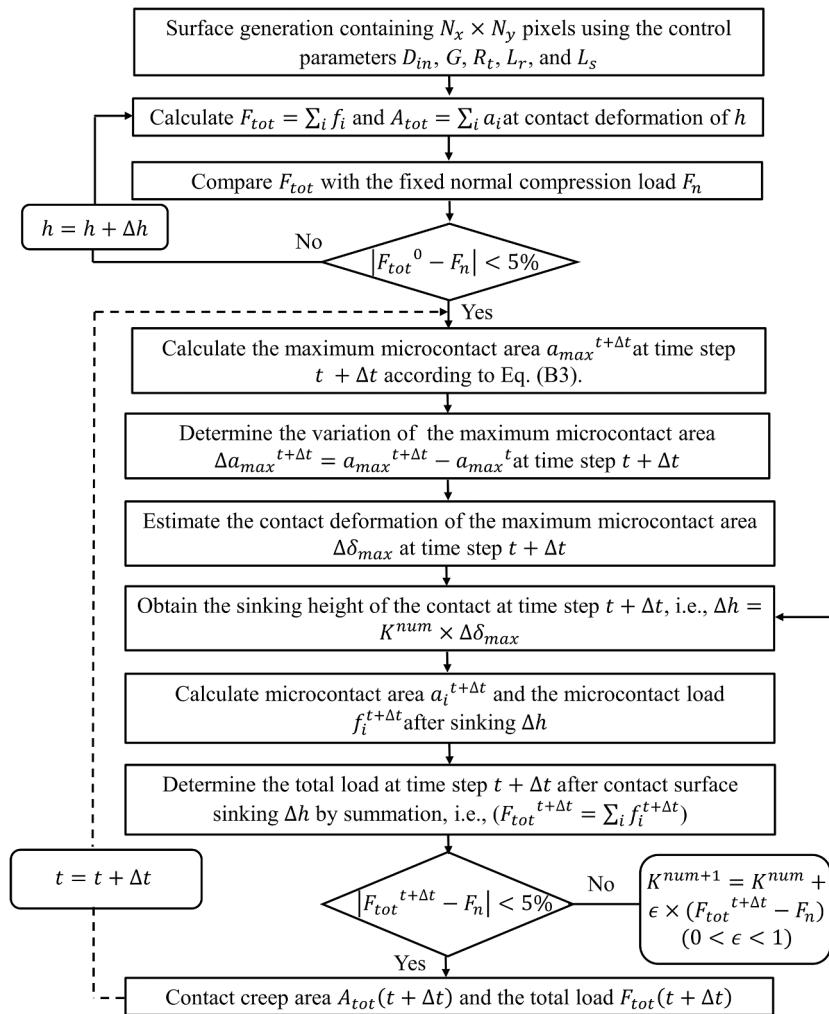
Fig. C1. Flow chart of numerical procedures for calculating the contact creep.

Appendix D

Digital volume correlation analyses

Digital Volume Correlation (DVC) is an optical flow-based image-matching technique that allows measuring the displacement and strain fields of a 3D object acquired at different loading steps. It can be used to follow *in-situ* or *ex-situ* mechanical tests or in general, any kind of deformation process that the object undergoes. Since the first application of DVC, several algorithms (Leclerc et al., 2011); (Madi et al., 2013); (Smith et al., 2002) have been developed, capable of achieving high accuracy and precision in displacement and small strains. In this study, two techniques are used to measure specimen deformation including a traditional subset-based approach (''local'') and a more robust technique based on finite-element (''global''). The ''global'' DVC technique assumes that the measured displacement field is continuous, which allows for a more accurate and robust result close to the solution. However, it relies on a linear problem inversion, which can be more costly than the resolution techniques used in the traditional subset-based techniques where the subsets are individually correlated. For this reason, a subset-based approach is advised in the case of ''large'' expected displacements between two images (typically > 10 voxels), allowing the initialization of the more robust ''global'' technique.

The principle of the generalized algorithm is as follows. The two 3D images to be correlated are denoted as $f(x)$ (the reference image) and $g(x)$ (the deformed image), where f and g are scalar gray levels at each voxel location x. Fundamentally, DVC rests on the basic assumption that upon a mere change in the position of voxels, defined by a displacement field $u(x)$, the two images can be brought to perfect coincidence such that

$$f(x) = g(x + u(x)) \tag{D1}$$

which should be close to imaging noise. However, in practice, $u(x)$ may assume arbitrary values, and hence it is essential to provide an estimate of the gray level at an arbitrary position. A worthwhile approach is to assume that $u(x)$ is known, how credible is it to measure locally a gray level f on one voxel, and to estimate (via interpolation)$g(x + u(x))$ at the same position, after displacement correction. For any displacement field $u(x)$, one may construct a corrected image $g(x + u(x))$, and thus a cost function

$$\mathscr{T}_{DVC}[u] = S(f, g). \tag{D2}$$

Solving this equation is equivalent to minimizing the cost function $\mathcal{T}_{DVC}[\boldsymbol{u}]$.

Appendix E

Correlation between contact strain and roughness at non-contacting zones

In the present experiment, we also observe that the surface geometrical feature also plays a central role in controlling contact strain. To quantify the influence of roughness at non-contacting zones on contact deformation over time, we examine the correlation between local contact strain and roughness features, including κ_{xy} and g_{surf}. We only include points with the E_{Mises} greater than the mean value by 5 % for all chosen surficial pixels in correlation analysis. The values of E_{Mises} of surficial points are extracted at the fifth XRCT measurement step with respect to the first measurement step, and the values of κ_{xy} and g_{surf} are calculated based on the surface structure reconstructed in the first XRCT measurement step. The correlation analyses between κ_{xy} and E_{Mises} for different specimens are shown in the first line of Fig. E1. The observed positive correlations across all samples indicate that locations exhibiting convex tend to deform more than concave locations. The correlation analyses between g_{surf} and E_{Mises} for different specimens are provided in the second row of Fig. E1, where the surface gradient is negatively correlated with the pixel strain. This means creep appears to be less significant at locations with steep slopes, for a given surface. Trends shown in Fig. E1 are consistent across all surfaces with different values of R_{rms} and D_{box}, though the obtained correlation coefficients are typically lower than 0.25. Results shown in Figs. 7-9 (in the main manuscript), and E1 suggest that strain and roughness features at non-contacting zones influence each other during the creep process.
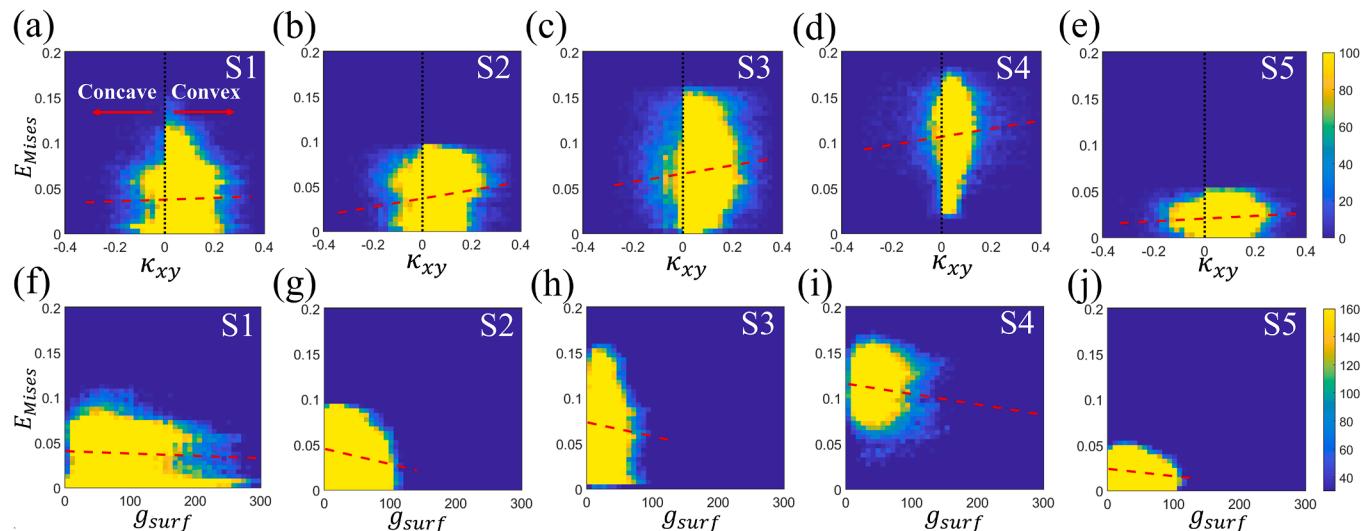

Fig. E1. The joint density map between the von Mises strain and horizontal local curvature and surface gradient . (a-e) Positive (Negative) curvature represents convex (concave) in locality. (f-j) The greater the surface gradient , the steeper the locality. The red dotted line is the linear fitting curve, and vertical lines drawn by black dots indicate zero curvature.

References

Alaboodi, A.S., Sivasankaran, S., 2018. Experimental design and investigation on the mechanical behavior of novel 3D printed biocompatibility polycarbonate scaffolds for medical applications. J. Manuf. Process. 35, 479–491.

Barba, D., Arias, A., Garcia-Gonzalez, D., 2020. Temperature and strain rate dependences on hardening and softening behaviours in semi-crystalline polymers: application to PEEK. Int. J. Solids Struct. 182, 205–217.

Bay, B.K., Smith, T.S., Fyhrie, D.P., Saad, M., 1999. Digital volume correlation: three-dimensional strain mapping using X-ray tomography. Exp. Mech. 39 (3), 217–226.

Brechet, Y., Estrin, Y., 1994. The effect of strain rate sensitivity on dynamic friction of metals. Scripta Metallurgica Et Materialia; (United States) 30 (11).

Brot, C., Etsion, I., Kligerman, Y., 2008. A contact model for a creeping sphere and a rigid flat. Wear 265 (5–6), 598–605.

Cecchi, A., Tralli, A., 2012. A homogenized viscoelastic model for masonry structures. Int. J. Solids Struct. 49 (13), 1485–1496.

Chen, Z., Liu, Y., Zhou, P., 2018. A comparative study of fractal dimension calculation methods for rough surface profiles. Chaos Solitons Fractals 112, 24–30.

Cholleti, E.R., Stringer, J., Kelly, P., Bowen, C., Aw, K., 2021. Studying the creep behaviour of strechable capacitive sensor with barium titanate silicone elastomer composite. Sens. Actuators, A 319, 112560.

Ciavarella, M., Joe, J., Papangelo, A., Barber, J., 2019. The role of adhesion in contact mechanics. J. R. Soc. Interface 16 (151), 20180738.

Coble, R., 1963. A model for boundary diffusion controlled creep in polycrystalline materials. J. Appl. Phys. 34 (6), 1679–1682.

Conyers, H., 1950. Diffusional viscosity of a polycrystalline solid. J. Appl. Phys. 21 (5), 437–445.

Coulomb, C., 1785. The Theory of Simple Machines (in Frencth). Mem. Math. Phys. Acad. Sci 10, 161–331.

Cristescu, N. (1993). A general constitutive equation for transient and stationary creep of rock salt. International journal of rock mechanics and mining sciences & geomechanics abstracts.

De Santis, A., Fedi, M., Quarta, T. (1997). A revisitation of the triangular prism surface area method for estimating the fractal dimension of fractal surfaces.

Depiver, J.A., Mallik, S., Harmanto, D. (2021). Solder joint failures under thermo-mechanical loading conditions–a review. Advances in Materials and Processing Technologies, 7(1), 1-26.

Dubuc, B., Quiniou, J., Roques-Carmes, C., Tricot, C., Zucker, S., 1989. Evaluating the fractal dimension of profiles. Phys. Rev. A 39 (3), 1500.

Dwyer-Joyce, R., Drinkwater, B., Quinn, A., 2001. The use of ultrasound in the investigation of rough surface interfaces. J. Trib. 123 (1), 8–16.

Fu, K., Sheppard, L.R., Chang, L., An, X., Yang, C., Ye, L., 2018. Length-scale-dependent nanoindentation creep behaviour of Ti/Al multilayers by magnetron sputtering. Mater Charact 139, 165–175.

Gallant, J.C., Moore, I.D., Hutchinson, M.F., Gessler, P., 1994. Estimating fractal dimension of profiles: a comparison of methods. Math. Geol. 26, 455–481.

Garofalo, F., 1963. An empirical relation defining the stress dependence to minimum creep rate in metals. Trans. Metall. Soc. AIME 227, 351.

Garofalo, F. (1965). Fundamentals of creep and creep-rupture in metals(Creep and creep rupture in metals and alloys, fundamental information for instruction and reference). New York, Macmillan Co., London, Collier- Macmillan, Ltd., 1965. 258 P.

Ghaednia, H., Pope, S.A., Jackson, R.L., Marghitu, D.B., 2016. A comprehensive study of the elasto-plastic contact of a sphere and a flat. Tribol. Int. 93, 78–90. https://doi.org/10.1016/j.triboint.2015.09.005.

Goedecke, A., Mock, R. (2009). Creep relaxation of an elastic–perfectly plastic hemisphere in fully plastic contact.

Goedecke, A., Jackson, R.L., Bachmaier, G., 2014. Time-dependent contact resistance in a multi-scale surface model. ICEC 2014; the 27th International Conference on Electrical Contacts.

Gonzalez-Valadez, M., Baltazar, A., Dwyer-Joyce, R.S., 2010. Study of interfacial stiffness ratio of a rough surface in contact using a spring model. Wear 268 (3–4), 373–379. https://doi.org/10.1016/j.wear.2009.08.022.

Gonzalez-Valadez, M., Dwyer-Joyce, R.S., 2009. Asperity creep measured by the reflection of ultrasound at rough surface contact. J. Tribol. 131 (2) https://doi.org/10.1115/1.3089217.

Greenwood, J.A., Williamson, J.P., 1966. Contact of nominally flat surfaces. Proc. R. Soc. Lond. A 295 (1442), 300–319.

Gregori, G., Clarke, D.R., 2006. The interrelation between adhesion, contact creep, and roughness on the life of gold contacts in radio-frequency microswitches. J. Appl. Phys. 100 (9), 094904.

He, H., Chen, W., Yin, Z.-Y., Senetakis, K., Yin, J.-H., 2021. A micromechanical-based study on the tribological and creep-relaxation behavior of sand-FRP composite interfaces. Compos. Struct. 275, 114423.

Hill, R., 1948. A theory of the yielding and plastic flow of anisotropic metals. Proc. R. Soc. Lond. A 193 (1033), 281–297.

Hurley, R.C., Pagan, D.C., Herbold, E.B., Zhai, C., 2023. Examining the micromechanics of cementitious composites using In-Situ X-ray measurements. Int. J. Solids Struct. 267, 112162.

Jeng, Y.-R., Peng, S.-R. (2006). Elastic-plastic contact behavior considering asperity interactions for surfaces with various height distributions.

Jia, S., Wen, C., Wu, B., 2020. A nonlinear elasto-viscoplastic model for clayed rock and its application to stability analysis of nuclear waste repository. Energy Sci. Eng. 8 (1), 150–165.

Kassner, M.E., 2015. Fundamentals of creep in metals and alloys. Butterworth-Heinemann.

Klinkenberg, B., Goodchild, M., 1992. The fractal properties of topography: a comparison of methods. Earth Surf. Proc. Land. 17 (3), 217–234.

Komvopoulos, K., 2020. A multiscale theoretical analysis of the mechanical, thermal, and electrical characteristics of rough contact interfaces demonstrating fractal behavior. Frontiers in Mechanical Engineering 6. https://doi.org/10.3389/fmech.2020.00036.

Larsson, J., Biwa, S., Storåkers, B., 1999. Inelastic flattening of rough surfaces. Mech. Mater. 31 (1), 29–41.

Leclerc, H., Périé, J.-N., Roux, S., Hild, F., 2011. Voxel-scale digital volume correlation. Experimental Mechanics 51 (4), 479–490.

Li, J., Du, Q., Sun, C., 2009. An improved box-counting method for image fractal dimension estimation. Pattern Recogn. 42 (11), 2460–2469.

Li, L.-T., Liang, X.-M., Xing, Y.-Z., Yan, D., Wang, G.-F., 2021. Measurement of real contact area for rough metal surfaces and the distinction of contribution from elasticity and plasticity. J. Tribol. 143 (7).

Li, S., Yao, Q., Li, Q., Feng, X.-Q., Gao, H., 2018. Contact stiffness of regularly patterned multi-asperity interfaces. J. Mech. Phys. Solids 111, 277–289. https://doi.org/10.1016/j.jmps.2017.10.019.

Liu, D., Yu, J., 2009. Otsu method and K-means. 2009 Ninth International Conference on Hybrid Intelligent Systems.

Liu, J.-L., Yu, Z.-G., Anh, V., 2014. Topological properties and fractal analysis of a recurrence network constructed from fractional Brownian motions. Phys. Rev. E 89 (3), 032814.

Madi, K., Tozzi, G., Zhang, Q., Tong, J., Cossey, A., Au, A., Hollis, D., Hild, F., 2013. Computation of full-field displacements in a scaffold implant using digital volume correlation and finite element analysis. Med. Eng. Phys. 35 (9), 1298–1312.

Meng, Q., Wang, Z., 2019. Creep damage models and their applications for crack growth analysis in pipes: a review. Eng. Fract. Mech. 205, 547–576. https://doi.org/10.1016/j.engfracmech.2015.09.055.

Merola, M., Ruggiero, A., De Mattia, J.S., Affatato, S., 2016. On the tribological behavior of retrieved hip femoral heads affected by metallic debris. A comparative investigation by stylus and optical profilometer for a new roughness measurement protocol. Measurement 90, 365–371.

Michalowski, R.L., Wang, Z., Nadukuru, S.S., 2018. Maturing of contacts and ageing of silica sand. Géotechnique 68 (2), 133–145. https://doi.org/10.1680/jgeot.16.P.321.

Michopoulos, J.G., Young, M., Iliopoulos, A., 2015. A multiphysics theory for the static contact of deformable conductors with fractal rough surfaces. IEEE Trans. Plasma Sci. 43 (5), 1597–1610.

Nayak, S.R., Mishra, J., Palai, G., 2019. Analysing roughness of surface through fractal dimension: a review. Image Vis. Comput. 89, 21–34.

Ng, H., Ong, S., Foong, K., Goh, P.-S., Nowinski, W., 2006. Medical image segmentation using k-means clustering and improved watershed algorithm. 2006 IEEE Southwest Symposium on Image Analysis and Interpretation.

Nix, W., Gibeling, J., Raj, R., 1985. Flow and fracture at elevated temperatures. 1983 ASM Materials Science Seminar.

Oliver, W.C., Pharr, G.M., 2004. Measurement of hardness and elastic modulus by instrumented indentation: Advances in understanding and refinements to methodology. J. Mater. Res. 19 (1), 3–20.

Olsson, E., Larsson, P.L., 2013. Jul). A numerical analysis of cold powder compaction based on micromechanical experiments. Powder Technol. 243, 71–78. https://doi.org/10.1016/j.powtec.2013.03.040.

Ovcharenko, A., Halperin, G., Etsion, I., Varenberg, M., 2006. A novel test rig for in situ and real time optical measurement of the contact area evolution during pre-sliding of a spherical contact. Tribol. Lett. 23 (1), 55–63.

Panigrahy, C., Seal, A., Mahato, N.K., Bhattacharjee, D., 2019. Differential box counting methods for estimating fractal dimension of gray-scale images: a survey. Chaos Solitons Fractals 126, 178–202.

Parland, H., 1995. Stability of rigid body assemblages with dilatant interfacial contact sliding. Int. J. Solids Struct. 32 (2), 203–234.

Pawlus, P., Reizer, R., Wieczorowski, M., 2017. Problem of non-measured points in surface texture measurements. Metrology and Measurement Systems 24 (3).

Pawlus, P., Reizer, R., Wieczorowski, M., 2018. Comparison of results of surface texture measurement obtained with stylus methods and optical methods. Metrology and Measurement Systems 25 (3).

Persson, B.N., 2001. Theory of rubber friction and contact mechanics. J. Chem. Phys. 115 (8), 3840–3861.

Persson, B.N.J., 2014. On the fractal dimension of rough surfaces. Tribol. Lett. 54 (1), 99–106. https://doi.org/10.1007/s11249-014-0313-4.

Pilvelait, T., Dillavou, S., Rubinstein, S.M., 2020. Influences of microcontact shape on the state of a frictional interface. Physical Review Research 2 (1). https://doi.org/10.1103/PhysRevResearch.2.012056.

Poon, C.Y., Bhushan, B., 1995. Comparison of surface roughness measurements by stylus profiler AFM and non-contact optical profiler. Wear 190 (1), 76–88.

Popov, V.L., Dimaki, A., Psakhie, S., Popov, M., 2015. On the role of scales in contact mechanics and friction between elastomers and randomly rough self-affine surfaces. Sci. Rep. 5 (1), 11139.

Rezvanian, O., Brown, C., Zikry, M., Kingon, A., Krim, J., Irving, D., Brenner, D., 2008. The role of creep in the time-dependent resistance of Ohmic gold contacts in radio frequency microelectromechanical system devices. J. Appl. Phys. 104 (2), 024513.

Rong, W., Li, Z., Zhang, W., Sun, L., 2014. An improved CANNY edge detection algorithm. 2014 IEEE International Conference on Mechatronics and Automation.

Sandström, R., 2018. Fundamental models for the creep of metals. Creep 239.

Sangeetha, D., Deepa, P., 2019. FPGA implementation of cost-effective robust Canny edge detection algorithm. J. Real-Time Image Proc. 16, 957–970.

Sevostianov, I., Kachanov, M., 2008. Contact of rough surfaces: a simple model for elasticity, conductivity and cross-property connections. J. Mech. Phys. Solids 56 (4), 1380–1400.

Smith, T.S., Bay, B.K., Rashid, M.M., 2002. Digital volume correlation including rotational degrees of freedom during minimization. Exp. Mech. 42 (3), 272–278.

Sofonea, M., Matei, A. (2012). Mathematical models in contact mechanics (Vol. 398). Cambridge University Press.

Spurr, R., 1955. Creep and static friction. Br. J. Appl. Phys. 6 (11), 402.

Stamati, O., Andò, E., Roubin, E., Cailletaud, R., Wiebicke, M., Pinzon, G., Couture, C., Hurley, R.C., Caulk, R., Caillerie, D., 2020. Spam: software for practical analysis of materials. Journal of Open Source Software 5 (51), 2286.

Storåkers, B., Biwa, S., Larsson, P.-L., 1997. Similarity analysis of inelastic contact. Int. J. Solids Struct. 34 (24), 3061–3083.

Ta, W., Qiu, S., Wang, Y., Yuan, J., Gao, Y., Zhou, Y., 2021. Volumetric contact theory to electrical contact between random rough surfaces. Tribol. Int. 160, 107007.

Taillandier-Thomas, T., Roux, S., Morgeneyer, T.F., Hild, F., 2014. Localized strain field measurement on laminography data with mechanical regularization. Nucl. Instrum. Methods Phys. Res., Sect. B 324, 70–79.

Talebinejad, M., Chan, A.D., Miri, A., Dansereau, R.M., 2009. Fractal analysis of surface electromyography signals: a novel power spectrum-based method. J. Electromyogr. Kinesiol. 19 (5), 840–850.

Taylor, R.I., 2022. Rough surface contact modelling—a review. Lubricants 10 (5). https://doi.org/10.3390/lubricants10050098.

Wang, W., Buhl, P., Klenk, A., Liu, Y., 2016. The effect of in-service steam temperature transients on the damage behavior of a steam turbine rotor. Int. J. Fatigue 87, 471–483.

Wang, X., Zhai, C., Gan, Y., 2021. Stress-dependent electrical impedance behaviours at fractal rough interfaces. Surf. Topogr. Metrol. Prop. 9 (2) https://doi.org/10.1088/2051-672X/abf84f.

Wang, R., Zhu, L., Zhu, C., 2017. Research on fractal model of normal contact stiffness for mechanical joint considering asperity interaction. Int. J. Mech. Sci. 134, 357–369. https://doi.org/10.1016/j.ijmecsci.2017.10.019.

Yan, W., Komvopoulos, K., 1998. Contact analysis of elastic-plastic fractal surfaces. J. Appl. Phys. 84 (7), 3617–3624. https://doi.org/10.1063/1.368536.

Yastrebov, V.A., Anciaux, G., Molinari, J.-F., 2015. From infinitesimal to full contact between rough surfaces: Evolution of the contact area. Int. J. Solids Struct. 52, 83–102. https://doi.org/10.1016/j.ijsolstr.2014.09.019.

Yeo, C.-D., Katta, R.R., Lee, J., Polycarpou, A.A., 2010. Effect of asperity interactions on rough surface elastic contact behavior: hard film on soft substrate. Tribol. Int. 43 (8), 1438–1448.

Zhai, C., Hanaor, D., Proust, G., Brassart, L., Gan, Y., 2016. Interfacial electro-mechanical behaviour at rough surfaces. Extreme Mech. Lett. 9, 422–429. https://doi.org/10.1016/j.eml.2016.03.021.

Zhai, C., Hanaor, D., Gan, Y., 2017. Contact stiffness of multiscale surfaces by truncation analysis. Int. J. Mech. Sci. 131–132, 305–316. https://doi.org/10.1016/j.ijmecsci.2017.07.018.

Zhai, C., Hanaor, D., Proust, G., Gan, Y., 2017. Stress-dependent electrical contact resistance at fractal rough surfaces. J. Eng. Mech. 143 (3), B4015001.

Zhai, C., Herbold, E., Hall, S., Hurley, R., 2019. Particle rotations and energy dissipation during mechanical compression of granular materials. J. Mech. Phys. Solids 129, 19–38.

Zhai, C., Pagan, D., Hurley, R., 2020. In situ X-ray tomography and 3D X-ray diffraction measurements of cemented granular materials. JOM 72, 18–27.

Zhai, C., Zhang, S., Ji, H., Wei, D., Song, H., Liu, K., Xu, M., 2023. Flexoelectricity at fractal rough surfaces. Extreme Mech. Lett. 101997.

Zhang, F., Liu, J., Ding, X., Wang, R., 2019. Experimental and finite element analyses of contact behaviors between non-transparent rough surfaces. J. Mech. Phys. Solids 126, 87–100. https://doi.org/10.1016/j.jmps.2019.02.004.

Zhao, Y., Chang, L., 2001. A model of asperity interactions in elastic-plastic contact of rough surfaces. J. Tribol. 123 (4), 857–864. https://doi.org/10.1115/1.1338482.